

Multi-Scale Modelling of Cavitation-Induced Pressure Around the Delft Twist 11 Hydrofoil

Artur K. Lidtke¹, Stephen R. Turnock¹, Victor F. Humphrey²

(¹Fluid-Structure Interactions Group, University of Southampton, UK ²Institute of
Sound and Vibration Research (ISVR), University of Southampton, UK)

ABSTRACT

A hybrid Lagrangian-Eulerian cavitation model based on the Schnerr-Sauer mass-transfer formulation is developed and then applied to study the flow around the Delft Twist 11 hydrofoil. The model uses volume-of-fluid approach to resolve large cavities and uses an interface reconstruction algorithm to identify vapour structures smaller than a grid-related threshold. These are then transferred to a Lagrangian framework and convected as particles acting as point noise sources. The underlying volume-of-fluid (VOF) model is shown to be in qualitatively good agreement with the experiment although it is found to under-predict the extent of cavitation. The combined model shows a substantial improvement in the prediction of near-field pressure fluctuations by accounting for the broadband contribution of bubbles smaller than the Eulerian grid size. In the pressure fluctuation spectra this is seen as a plateau extending to over a kilohertz beyond the low-frequency harmonics associated with the shedding frequency.

INTRODUCTION

Recent years have seen a surge of interest in the development of a better understanding of the input of noise into the oceans. This is evident, for instance, in the European Union initiatives such as AQUO and SONIC (EU FP7, 2014a,b). Out of the anthropogenic noise sources possibly affecting marine life shipping is thought to contribute significantly to the overall sound pressure levels (Hildebrand, 2009, Urik, 1984).

The propeller is usually responsible for most of the sound generated by a ship under way (Bertschneider et al., 2014). Typically, it is the cavitation phenomenon that tends to dominate the radiated noise spectrum (Brooker and Humphrey, 2014). This set of noise mechanisms may be broadly divided into high-frequency

components, associated with vortex cavitation and shock wave formation, and low-frequency noise due to fluctuation of cavity volume due to the propeller blade changing its loading over one shaft revolution (Park et al., 2009a, Seol et al., 2005). The latter are typically of more interest from an environmental protection point of view since low-frequency noise is attenuated less and thus affects a much larger area.

Experimental measurements of ship and propeller noise, both at full- and model-scales, are well established and widely used (Aktas et al., 2015, Bertschneider et al., 2014, Brooker and Humphrey, 2014). Nonetheless, issues remain, particularly when it comes to scaling model data to make full-scale predictions. Numerical methods have, therefore, started to gain attention as they can potentially offer an alternative source of insight into the flow at a much reduced cost. Several authors have reported using computational fluid dynamics (CFD), typically in conjunction with acoustic analogies, in order to model the noise radiated by hydrofoils, propellers and appended ship hulls (Ianniello et al., 2013, Ianniello and Bernardis, 2015, Lloyd et al., 2015, Seol et al., 2005). Attempts have also been made at modelling cavitation noise using similar approaches (Lidtke et al., 2016, Seo et al., 2008, Seol, 2013).

However, most of the traditional volume-of-fluid (VOF) and level-set based cavitation models are incapable of accounting for the high-frequency or broadband cavitation noise. Firstly, because they usually do not account for compressibility and thus do not resolve the shock waves associated with collapses. Secondly, most numerical codes relying on Eulerian grids will find it difficult to accurately resolve collapse mechanisms, which may take place on the length-scales of the order of a micron. This becomes increasingly problematic as one considers that cavitation often occurs some distance away from solid walls where numerical grids tend to be coarser.

An implementation of a multi-scale Euler-Lagrange model in OpenFOAM® 3.0.1 has been developed and is proposed as a potential solution to overcome the aforementioned difficulty, thus paving the way for accurate modelling of both far-field and near-field cavitation noise. Doing so allows for a much better matching of CFD with experimental observations in cavitation tunnels, possibly allowing CFD to be more readily usable in marine noise predictions. Hybrid cavitation models are not a completely novel concept and have been used to study erosion and, to a lesser extent, radiated noise (Hsiao et al., 2014, Vallier, 2013, Yakubov et al., 2013). The present work, however, attempts to approach the problem strictly with the aim of complementing noise measurements in cavitation tunnels and at full scale. The Delft Twist 11 hydrofoil has been chosen as a well-studied, both experimentally and numerically, representative test case (Bensow, 2011, Foeth et al., 2006, Foeth, 2008, Hoekstra et al., 2011). In more detail, the objectives of the study were to first establish grid independence using steady-state results with a RANS model and compare these against experimental data in non-cavitating conditions. Then, cavitation predictions using a standard mass-transfer model were made in order to study the cavity shape and location, sheet cycle frequency, and pressures induced at the wall of the tunnel. Finally, the cavitation simulation was re-evaluated using a hybrid Lagrangian-Eulerian bubble tracking model in order to investigate where the bubbles get injected into the flow and how this compares with experimental photographs, as well as how the broadband noise from the small bubbles affects the wall pressures.

METHODOLOGY

Test case

In all of the simulations half of the original twisted foil geometry studied experimentally by Foeth (2008) has been studied. It consists of a NACA0009 foil with varying twist angle along the span, yielding an angle of attack of -2 degrees at the wall of the cavitation tunnel up to 9 degrees at the centreline. While the considered geometry is relatively simple, the test case is subject to significant sheet cavitation, making it representative of some of the key modelling challenges found on a marine propeller. A summary of the test conditions, as well as certain cavitation model settings, is presented in Table 1. The nuclei density and diameter were chosen based on a study by Bensow (2011). The choice of these values will affect the cavitation model results but lack of experimental measurements of these quantities forces the use of likely instead of exact parameters.

Computational grids

Structured hexahedral numerical grids were used in all investigations. The baseline mesh was designed to have $y^+ \leq 1.0$ with 3.6 million elements and was then subject to uniform refinement up to 3 times, yielding a grid with just under 30 million cells. The medium, or 7.3 million element, mesh only was used in the cavitation simulations. This had a medium x^+ of 230 and z^+ of 300 with 150 cells along the span of the foil.

Table 1: Summary of the dimensions of the foil and the flow properties used Bensow (2011), Foeth (2008), Hoekstra et al. (2011).

Parameter	Value	Unit
Chord (c)	0.15	m
Angle of attack (mid-span)	9	deg
Span (s)	0.3	m
Inlet velocity	6.97	m s^{-1}
Outlet pressure	29	kPa
Cavitation number, σ	1.07	-
Water density, ρ_l	998	kg m^{-3}
Vapour density, ρ_v	0.023	kg m^{-3}
Water kinematic viscosity, ν_l	$0.923 \cdot 10^{-6}$	$\text{m}^2 \text{s}^{-1}$
Vapour kinematic viscosity, ν_v	$4.273 \cdot 10^{-6}$	$\text{m}^2 \text{s}^{-1}$
Mean nucleation radius, R_0	50	μm
Nuclei density, n_0	10^8	m^{-3}
Saturated vapour pressure	2970	Pa
Schnerr-Sauer tuning coeff.	1.0	-
Inlet ν_T	$1.28 \cdot 10^{-4}$	$\text{m}^2 \text{s}^{-1}$

The upstream domain extent was chosen to be 2 chord lengths (c) away from the leading edge and 6 c downstream of the trailing edge. Vertically the domain extended 1 c on either side of the foil in order to replicate the blockage experienced in the experiments. In the publicly available geometry the foil has a sharp trailing edge approximately 0.4 mm thick. In the present simulation this was replaced with a round profile, allowing a higher quality numerical grid to be created. It is believed that this would have a minimal effect on the dominant cavitation flow features located around the leading edge. The downstream part of the mesh was aligned with local flow by applying a span-wise twist to the mesh blocks based on the results of preliminary computations. An overview of the mesh used for cavitation simulations is shown in Figure 1.

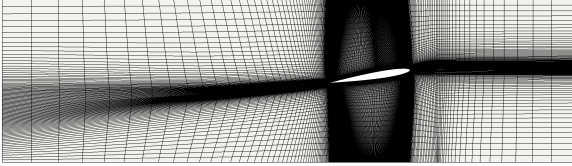
Turbulence model

Incompressible flow is assumed in all of the presented Eulerian simulations, which is governed by the

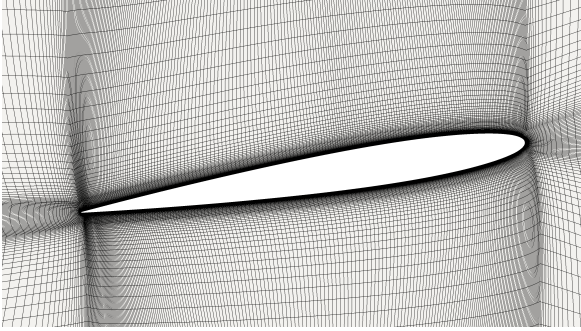
momentum and mass conservation equations,

$$\begin{aligned} \frac{\partial \mathbf{U}}{\partial t} + \nabla \cdot (\mathbf{U} \otimes \mathbf{U}) &= -\frac{1}{\rho} \nabla p + \nu \mathbf{D}, \\ \nabla \cdot \mathbf{U} &= 0, \end{aligned} \quad (1)$$

where \mathbf{U} is the flow velocity, p , is the pressure, ν is the kinematic viscosity, ρ is the density, and \mathbf{D} is the deviatoric stress tensor.



a) Computational domain and wake adaptation of the mesh



b) O-grid mesh topology around the foil

Figure 1: Details of the 7 million cells mesh at the mid-span of the foil.

The presented non-cavitating flow simulations make use of the Reynolds-Averaged Navier Stokes (RANS) approach with the time-dependence of the problem ignored. In the RANS method mean values of the flow quantities are solved for, which gives rise to an additional stress term which needs to be accounted for in order to close the system of equations. In the present work the Spalart and Allmaras (1992) model, based on the Boussinesq assumption, is used for that purpose. In this framework a single additional variable, $\hat{\nu}$, is solved for, assuming it obeys an equation of form

$$\begin{aligned} \frac{\partial \hat{\nu}}{\partial t} + \nabla \cdot (\mathbf{U} \hat{\nu}) &= c_{b1} \hat{S} \hat{\nu} - c_{w1} f_w \left(\frac{\hat{\nu}}{d} \right)^2 \\ &+ \frac{1}{\sigma} \left[\nabla \cdot ((\nu + \hat{\nu}) \nabla \hat{\nu}) + c_{b2} (\nabla \hat{\nu})^2 \right], \end{aligned} \quad (2)$$

with details of the constants discussed at length in the original reference. Once $\hat{\nu}$ has been obtained, the turbulent eddy viscosity may be obtained using

$$\mu_t = \rho \hat{\nu} f_{v1} \quad (3)$$

as a function of $\chi = \hat{\nu}/\nu$ and

$$f_{v1} = \frac{\chi^3}{\chi^3 + c_{v1}^3}. \quad (4)$$

In order to better account for the unsteadiness of the flow, the cavitating simulations utilise the Delayed Detached Eddy Simulation (DDES) model based on the Spalart-Allmaras RANS formulation (Spalart and Allmaras, 1992). In this approach the RANS equation is solved in the attached boundary layer and gets blended into a Large Eddy Simulation (LES) formulation further away from the solid wall. This is done based on defining a limiting length for which RANS equation is solved, $l_{DES} = \min(d_w, C_{DES} \Delta)$ dependent on the wall distance d_w , a constant C_{DES} , and grid size Δ . This gives rise to issues for cells inside the boundary layer if the numerical mesh is fine (Spalart and Allmaras, 1992) and hence a fix has been used to delay the transition to the LES mode by the use of additional blending functions similar to the ones used in the shear stress transport (SST) RANS model (Menter et al., 2003).

Once in pure LES mode, the turbulence model solves filtered Navier-Stokes and continuity equations,

$$\begin{aligned} \frac{\partial \bar{\mathbf{U}}}{\partial t} + \nabla \cdot (\bar{\mathbf{U}} \otimes \bar{\mathbf{U}}) &= -\frac{1}{\rho} \nabla \bar{p} + \nu \nabla^2 \bar{\mathbf{U}} - \nabla \cdot \boldsymbol{\tau}, \\ \nabla \cdot \bar{\mathbf{U}} &= 0, \end{aligned} \quad (5)$$

where an overline notation denotes a filtered quantity and $\boldsymbol{\tau}$ is the non-linear subgrid stress tensor,

$$\boldsymbol{\tau} = \bar{\mathbf{U}} \otimes \bar{\mathbf{U}} - \bar{\mathbf{U}} \otimes \bar{\mathbf{U}}. \quad (6)$$

This is computed based on the eddy viscosity, thus providing a coupling between the resolved and unresolved turbulent scales. Filtering of the equations is done by multiplying the quantity in question with a convolution operator whose kernel is defined by the filter width related to the mesh size.

Mass transfer model

The Schnerr-Sauer cavitation model was used in the present study (Sauer and Schnerr, 2001). This model has reportedly been used to investigate unsteady cavitation behaviour with success, making it particularly appealing in the present application (Bensow, 2011, Koop, 2008, Vallier, 2013). The model depends on two primary constants, namely the nuclei density, n_0 , and mean nuclei radius, R_0 .

In the most basic sense, the cavitation model describes the rate of transfer of mass between the liquid and vapour phases, \dot{m} , which may also be interpreted as phase

change from liquid to vapour and *vice versa*. The used model approximates the behaviour of individual bubbles present in the fluid and being governed by the Rayleigh-Plesset equation (Plesset and Prosperetti, 1977, Sauer and Schnerr, 2001) and computes their equivalent mass transfer rate as

$$\dot{m} = C \frac{\rho_l \rho_v}{\rho} (1 - \alpha) \alpha \frac{3}{R} \sqrt{\frac{\frac{2}{3}(p - p_v)}{\rho_l}}, \quad (7)$$

where the radius R is modelled based on R_0 and n_0 , C is a constant tuning parameter set to 1.0 not to artificially alter the cavitation behaviour. In the actual implementation the mass transfer source term is split into condensation and vaporisation terms based on the sign of $p - p_v$.

The mass transfer rate is then used to modify the right-hand side of the scalar transport equation governing the liquid volume fraction,

$$\frac{\partial \alpha}{\partial t} + \nabla \cdot (\alpha \mathbf{U}) = -\frac{\dot{m}}{\rho}, \quad (8)$$

where α is the volume fraction, \mathbf{U} and ρ are the flow velocity and density, respectively.

Once this has been obtained for each time step, the density and viscosity of the fluid, ρ and μ , are interpolated in accordance with the mass conservative, immiscible fluid mixture assumption of the VOF method,

$$\phi = \alpha \phi_{liquid} + (1 - \alpha) \phi_{vapour}. \quad (9)$$

The pressure equation is also modified by introduction of the \dot{m} source term in order to account for a velocity divergence induced by the mass transfer, yielding

$$\nabla \cdot \bar{\mathbf{U}} = \left(\frac{1}{\rho_v} - \frac{1}{\rho_l} \right) \dot{m}. \quad (10)$$

Lagrangian-Eulerian cavitation model

The basic idea behind a hybrid Lagrangian-Eulerian cavitation model is to use the volume of fluid approach in order to model large-scale cavities but switch to treating them in the Lagrangian mode once they become too small to be accurately captured on the Eulerian grid. The latter involves tracking the bubbles in space based on their equation of motion

$$m_B \frac{d\mathbf{U}_B}{dt} = \mathbf{F}_a + \mathbf{F}_p + \mathbf{F}_{buoy} + \mathbf{F}_{drag} + \mathbf{F}_{lift}, \quad (11)$$

where m_B is the mass of a bubble with radius R and density ρ_B , \mathbf{U}_B is the velocity of the centre of mass of the bubble located at \mathbf{x}_B , and \mathbf{F} are individual force components. These correspond to added mass: $\mathbf{F}_a = \frac{1}{2} \rho \frac{m_B}{\rho_B} \left(\frac{D\mathbf{U}}{Dt} - \frac{d\mathbf{U}_B}{dt} \right)$,

pressure gradient: $\mathbf{F}_p = -\frac{m_B}{\rho_B} \nabla p$, buoyancy: $\mathbf{F}_{buoy} = m_B \left(1 - \frac{\rho}{\rho_B} \right) \mathbf{g}$, drag: $\mathbf{F}_{drag} = C_d \rho \frac{m_B}{\rho_B} \frac{3}{8R} (\mathbf{U} - \mathbf{U}_B) |\mathbf{U} - \mathbf{U}_B|$, and lift: $\mathbf{F}_{lift} = C_l \frac{m_B}{\rho_B} (\mathbf{U} - \mathbf{U}_B) \times \boldsymbol{\omega}$, where $\boldsymbol{\omega}$ is the vorticity (Hsiao et al., 2014, Nordin, 2001, Vallier, 2013, Yakubov et al., 2013). The lift coefficient, C_l is assumed to be constant and equal to 0.5, and the drag coefficient may be computed as a function of the Reynolds number of the bubble, $Re_B = 2|\mathbf{U} - \mathbf{U}_B|R/\nu$, as $C_d = 24.0/Re_B(1 + 0.15Re_B^{0.687})$ (Vallier, 2013).

During its lifetime a Lagrangian bubble experiences external pressure variations which affect its radius. This is governed by the Rayleigh-Plesset equation (Plesset and Prosperetti, 1977),

$$R\ddot{R} + \frac{3}{2}(\dot{R})^2 = \frac{1}{\rho} \left(p_B - p_{ext} - \frac{2\sigma_{st}}{R} - \frac{4\mu}{R}\dot{R} \right), \quad (12)$$

where the term p_B refers to the pressure inside the bubble consisting of the sum of the saturated vapour pressure, p_v , and the local gas pressure, p_g . R is the bubble radius, σ_{st} is the surface tension of the vapour and μ is its dynamic viscosity. p_{ext} is the pressure of fluid acting on the bubble which is assumed to be equal to the pressure at the bubble centre, in accordance with classical Lagrangian theory. A more accurate representation would be to compute average pressure over the bubble surface (Chahine, 2004), although this would result in an increased cost and code complexity and so is not done in the present model.

In order to account for the effect of compressibility of the gas enclosed inside the bubble the perfect gas relationship,

$$p_B = p_v + p_{g0} \left(\frac{R_0}{R} \right)^{3k}, \quad (13)$$

is used where p_{g0} is the equilibrium gas pressure in the bubble, R_0 and R are the equilibrium and current bubble radii, respectively, and k is the polytropic compression constant (Hsiao et al., 2014, Yakubov et al., 2013). The latter is assumed equal to 1.4 as for air undergoing an adiabatic process, which is more suitable for describing the bubble physics during collapse (Brennen, 2009b). For the growth phase assuming an isothermal process with $k = 1$ would be more appropriate but was neglected at this stage for simplicity.

As the bubble enters a collapse phase, which is detected as a high inwards velocity consistent over several consecutive integration time steps, liquid compressibility becomes important to the bubble physics, which gives rise to an alternative form of the Rayleigh-Plesset

equation,

$$R\ddot{R} \left[1 - (1 + \epsilon) \frac{\dot{R}}{c_0} \right] + \frac{3}{2} \dot{R} \left(\frac{4 - \epsilon}{3} - \frac{4}{3} \frac{\dot{R}}{c_0} \right) = \frac{1}{\rho} \left[p_v - p_{ext} - \frac{2\sigma_{st}}{R} + p_{gm} \left(\frac{R_{max}}{R} \right)^{3k} \right] + \frac{1}{\rho} \left[-3k p_{gm} \left(\frac{R_{max}}{R} \right)^{3k} + \frac{2\sigma_{st}}{R^2} \dot{R} \right], \quad (14)$$

expressed using the maximum radius, R_{max} and the corresponding non-condensable gas pressure, p_{gm} , while neglecting the effect of viscosity (Sunil et al., 2006, Tomita and Shima, 1977). In the above, $\epsilon = 1 = \rho_g/\rho \approx 0.99882$ is a function of the gas density under atmospheric conditions and water density, and c_0 is the speed of sound in water. It should be noted that Equation (14) reduces to (12) if one assumes $c_0 \rightarrow \infty$ and $\epsilon \rightarrow 1$.

As each bubble undergoes oscillation of its radius, it induces pressure fluctuations at an arbitrary point \mathbf{x} which may be described for a bubble at a point \mathbf{y} as (Brennen, 2009a, Hsiao and Chahine, 2008)

$$p \left(\mathbf{x}, t + \frac{c_0}{|\mathbf{x} - \mathbf{y}|} \right) = \frac{\rho}{|\mathbf{x} - \mathbf{y}|} \left(R^2 \ddot{R} + 2R\dot{R}^2 \right). \quad (15)$$

In order to arrive at a total pressure due to all the bubbles inside the numerical domain, each of their individual pressure signals must be interpolated onto a separate time axis corresponding to the receiver time, similarly as in the case of accounting for the retarded time in acoustic analogy formulations (Lidtke et al., 2016).

As a new Lagrangian bubble is created, its assumed to adopt an equilibrium pressure, p_{g0} , and radius, R_0 , when subject to the outlet pressure, p_{∞} . Furthermore, it is assumed that on the moment of creation the bubble is also in equilibrium under its current p_{ext} (Vallier, 2013). These two assumptions give rise an equilibrium relation,

$$\left(p_{\infty} - p_v \frac{2\sigma_{st}}{R_0} \right) \left(\frac{R_0}{R_{initial}} \right)^{3k} + p_v - \frac{2\sigma_{st}}{R_{initial}} - p_{ext} = 0, \quad (16)$$

which may be rearranged into a polynomial form and solved for the only unknown, R_0 , which is then used to determine p_{g0} in accordance with ideal gas law in Equation (13) (Vallier, 2013).

Following the initialisation, at the end of each CFD simulation time step the external liquid conditions at the bubble centre are determined using interpolation. Governing equations of motion, (11) and either (12) or (14), are integrated in time between the previous and current simulation times. For the Rayleigh-Plesset equations this is done by writing out a derivative vector of form $[\ddot{R}, \dot{R}]$ and integrating using the 4th-order Runge-Kutta method with adjustable time step. For the convection

equation an approach discussed by Nordin (2001) is followed, whereby the terms involving the continuous liquid phase are treated explicitly and implicit treatment is applied to the quantities associated with the bubble. This yields an expression which is then integrated using Euler method.

A critical step in the present model is determination where individual Lagrangian bubbles should be added. This first requires coherent cavitation structures to be reconstructed from the volume fraction field. This is done by first identifying all cells with liquid volume fraction $\alpha < \alpha_{threshold}$, where the threshold value of 0.8 is used. Setting too low a value would limit the number of particles being created but setting it too high could cause blending of the bubbles. This is a crucial parameter of the present model and hence future sensitivity studies are planned to investigate its effect. Once all vapour cells have been marked, one of them is selected at random and then a check is performed to establish if any of its neighbours are also filled with vapour. If yes, they are identified as a part of the same bubble. The process continues until no more cells may be added to the current bubble, at which point the next unassigned cell from the top list is chosen as a new starting point. The process continues until no more unassigned vapour cells exist in each sub-process domain.

In order to enable parallel running, the bubble connectivity information between each subdomain must be exchanged. This is done by first identifying each local bubble lying on the edge of the subdomain, denoted as a processor patch in OpenFOAM terminology and noting which processor it neighbours with. This gives rise to a list of tuples of local bubble identifiers and processor numbers they neighbour with and a list face identifiers for each candidate neighbour bubble. The lists are then gathered and scattered across all processes. Each individual processor then sorts through them and looks for bubbles in other domains which may potentially connect to its own cavity structures. For each of them, it compares the face identifiers of own candidate bubbles with those of cavities on the neighbouring domains. As soon as a match is found the two bubbles are marked as connected and this information is stored.

Once individual connectivity for all bubbles has been established, the information is exchanged again. At this stage properties of each of the subdomain bubbles,

such as centroid, volume and speed,

$$\begin{aligned}
 V_B &= \sum_I^{N_B} (1 - \alpha_I) V_{cell,I} \\
 \bar{\mathbf{x}}_B &= \frac{1}{V_B} \sum_I^{N_B} \mathbf{x}_{cell,I} (1 - \alpha_I) V_{cell,I} \\
 \mathbf{U}_B &= \frac{1}{V_B} \sum_I^{N_B} \mathbf{U}_I (1 - \alpha_I) V_{cell,I}
 \end{aligned} \quad (17)$$

may be added together to get a global picture. This yields a series of lists which allow net bubble properties to be associated with unique identifiers, shown in Figure 2 for an example time step of the present simulation.

The final step is to decide which bubbles should be transferred from the Eulerian to Lagrangian frame. This is done following an approach similar to Vallier (2013) and Tomar et al. (2010) where the bubbles were moved to the Lagrangian frame if the number of cells constituting them was less than a given threshold N_{EL} , assumed equal to 15 in the present study. A second criterion has also been added which compares the physical size of the bubble, taken as cube root of the total volume of cells across which it spans, $R_{swept} = (\sum_I^{N_B} V_{cell,I})^{1/3}$, to the mean grid size inside the bubble. If this satisfies $R_{swept}/\Delta_{mean} < 3$ as well as $N_B < N_{EL}$ then the bubble is added to the Lagrangian frame and the liquid fraction in the cells it used to occupy is set to 1. In order not to invalidate momentum conservation, the momentum the bubble exerts on the liquid should be accounted for in the form of a source term, thus providing two-way coupling (Tomar et al., 2010). For simplicity, one-way coupling has been used in the present study without affecting the momentum equation convergence, but the source-term approach is intended to be implemented in the future.

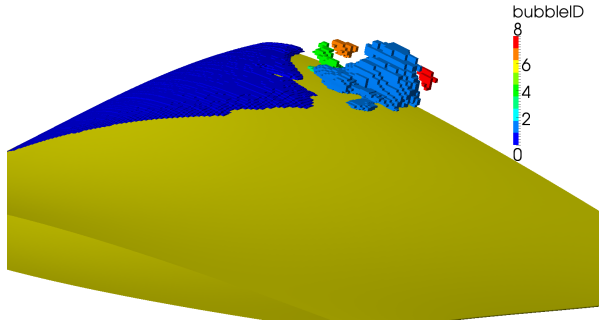


Figure 2: Example of cavities identified by the interface reconstruction algorithm during a simulation with 128 processors.

Numerical set up

The steady-state simulations were solved using the SIMPLE algorithm using second-order upwind convection scheme and first-order accuracy for the turbulent viscosity. Cavitation simulations were performed using the pressure implicit algorithm with splitting operators (PISO) with a fixed time step of $2.5 \cdot 10^{-6}$ seconds, corresponding to a maximum Courant number of approximately 0.5. An implicit second order backward time scheme was used, together with a second-order filtered-linear convection scheme. The volume of fluid field was discretised using the van Leer scheme and turbulent viscosity using an upwind stencil. The pressure equation was solved down to a residual of 10^{-6} and the volume of fluid equation down to 10^{-12} at each time step. The remaining fields were converged down to a residual of 10^{-9} . A preconditioned bi-conjugate gradient solver was used for all fields except pressure which was solved using a multi-grid solver. The boundary conditions used in the cavitation simulations are summarised in Table 2.

Table 2: Boundary conditions set-up for the cavitation simulations.

Boundary	U	p	α	\hat{v}
Inlet	Dirichlet	Neumann	Dirichlet	Dirichlet
Outlet	Neumann	Dirichlet	Neumann	Neumann
Foil	No-slip	Fixed flux	Neumann	Dirichlet
Sides	Slip	Neumann	Neumann	Neumann
Centreplane	Symmetry	Symmetry	Symmetry	Symmetry

Analysis

First, a range of steady-state RANS simulations was carried out on progressively refined meshes in order to study the effect of discretisation errors. This was then used to provide an initial condition for the cavitation simulation using the baseline Schnerr-Sauer model without Lagrangian bubble tracking. The simulation was run for four shedding cycles in order to remove initialisation transients, after which one second of data was obtained. During this time a particle of the fluid would be able to travel through the numerical domain 6.6 times with the inlet flow speed. Finally, the hybrid model was engaged and the simulation was subsequently run for four more shedding periods.

During each cavitation simulation the total volume of cavitation present in the numerical domain was monitored as

$$V = \sum_{i=0}^{N_{cells}} \frac{\min(0, \alpha_{threshold} - \alpha)}{|\alpha_{threshold} - \alpha|} (1.0 - \alpha) V_{cell,i}, \quad (18)$$

where $V_{cell,i}$ is the volume of a cell and $\alpha_{threshold}$ is a threshold value. Three different values were considered

here: 0.1, 0.5, and 0.9, where 1.0 corresponds to water with no vapour content.

The pressure on the walls of the numerical cavitation tunnel was monitored at six locations above the foil. These were placed by performing a linear projection of the pressure taps used in the experiment by Foeth (2008). Cartesian coordinates of the monitoring points are shown in Table 3.

Table 3: Locations of the probes placed to monitor pressures at the wall of the virtual cavitation tunnel. Origin at mid-chord, with x-axis pointing downstream and y-axis aligned with the span of the foil, as in Hoekstra et al. (2011).

Probe	x [m]	y [m]	z [m]
1	0.038	0.150	0.150
2	0.001	0.150	0.150
3	-0.013	0.150	0.150
4	-0.028	0.150	0.150
5	-0.043	0.150	0.150
6	-0.066	0.150	0.150

RESULTS

Non-cavitating flow

Figures 3 and 4 show the convergence of the steady force coefficient values and extremes of the pressure coefficient with varying the mesh size. It may be seen that for all but the coarsest mesh the relative change in the predictions is small.

The steady lift and drag coefficients predicted for the 7.3 million cell mesh were 0.423 and 0.0175, respectively. The experimental data only reports on the former, which for the considered case was measured to be 0.46, which stands in a rather large discrepancy to the results obtained here. Comparing the predicted values to the ones reported by participants of the 2011 SMP workshop (Hoekstra et al., 2011), a satisfactory agreement is seen with lift coefficients adopting values in the range 0.3653-0.4279 and the drag coefficient within 0.01447-0.0242. Given the grid independence of the current results, the likely reasons for the difference are the presence of natural laminar flow in the experiment and the fact that the boundary layer at the walls of the cavitation tunnel was not accounted for in the simulations.

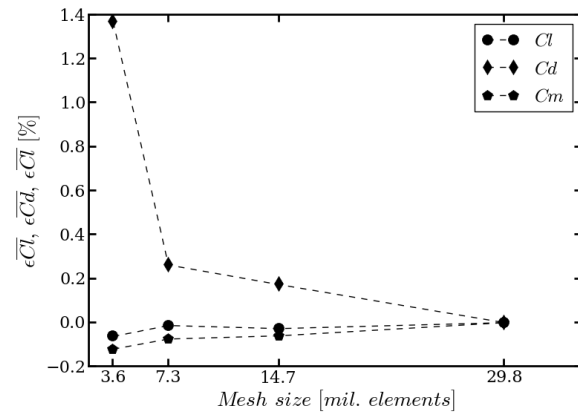


Figure 3: Convergence of the lift coefficient with increasing the cell count (finest mesh value used as reference).

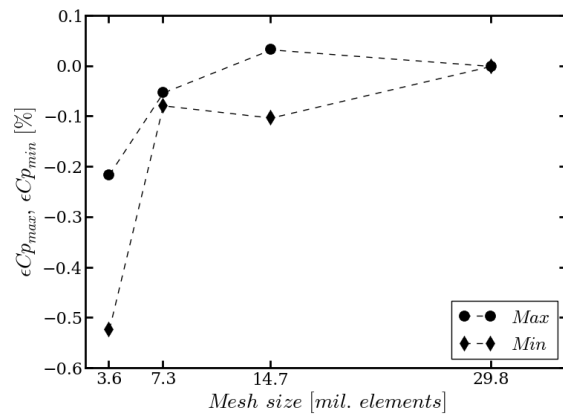


Figure 4: Convergence of the minimum pressure coefficient with increasing the cell count (finest mesh value used as reference).

Figure 5 depicts the steady lift coefficient distribution at several locations across the span of the foil as obtained using the 7.3 million cells mesh. Reasonable agreement is seen for all experimental data points on the suction surface, except for the one at $x/c=0.3$. It does appear to be a clear outlier, however, so the experimental accuracy at this location may be questioned. The predicted pressure coefficient at the bottom side of the foil appears to be higher than was reported in the experiment.

For the medium density mesh the predicted minimum pressure coefficient was -2.96. It is impossible to compare this with the experimental data due to the lack of a suitable measurement point. Numerical submissions to the 2011 SMP workshop, however, reported values between -3.17 and -3.23. This 6% difference is relatively small but could, in theory, lead to a smaller cavitation

extent in the present simulation by not inducing quite enough vaporisation near the leading edge of the foil.

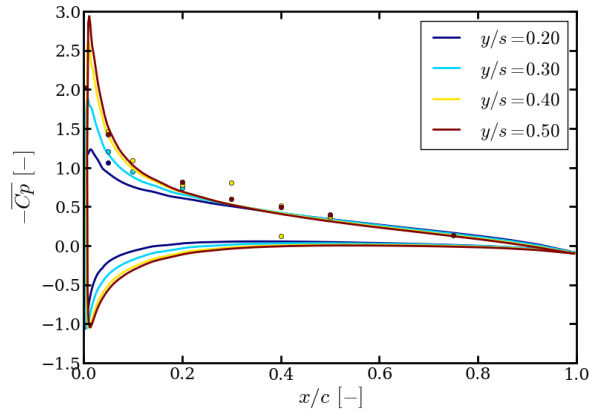


Figure 5: Comparison of the steady-state, non-cavitating pressure coefficient at various locations across the span with the experimentally reported values (Foeth, 2008).

Cavitation - flow field

For the baseline simulation of cavitating flow without Lagrangian bubble tracking the mean lift coefficient was 0.412. This stands in satisfactory agreement with values reported by Bensow (2011) who reported lift coefficient values between 0.42 and 0.45 for simulations using RANS, DES and LES. The experimental results, however, report the mean lift coefficient to have been 0.53 during the tests. The underestimation of lift suggests that the cavitation extent in the computations is too small.

Examining the mean pressure distribution at the mid-span of the foil in Figure 6 reveals just that. One may see how in the present results the characteristic plateau corresponding to the presence of a cavity sheet drops off around $x/c=0.3$, whereas in the experiment this was only reported to happen at $x/c=0.4$. In the measurement data the pressure coefficient also appears to have increased much more gradually in the region of cavity closure than what was observed in the current simulation.

Similar observation regarding the mean extent of the attached cavities may be drawn by examining the distribution of the average values of liquid volume fraction on the surface of the foil at mid-span, shown in Figure 7. It may be seen that the attached cavity does not extend further downstream than $x/c=0.3$. It is interesting to note that the mean value first nears pure water around $x/c=0.05$, then moves back towards vapour and only later moves to pure water region. This indicates that at some point during the cavitation cycle a gap exists between the attached cavity at the leading edge and one located further downstream.

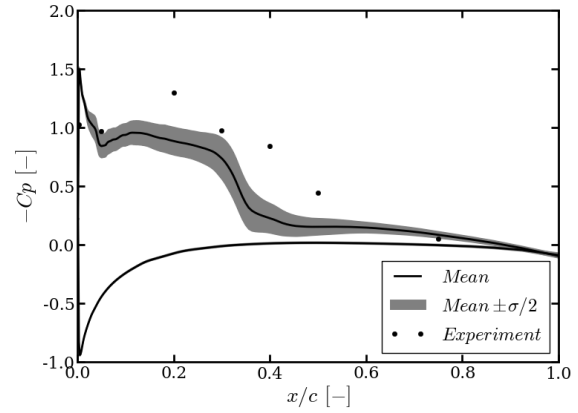


Figure 6: Mean pressure coefficient in cavitating condition, also showing the standard deviation and experimental data by Foeth (2008).

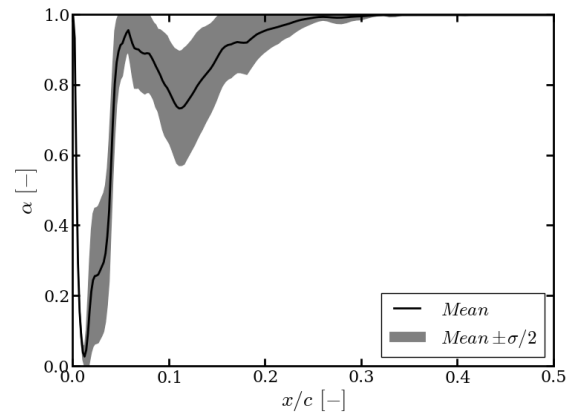


Figure 7: Mean volume fraction on the surface of the foil, also showing the standard deviation.

Looking at a mean distribution of α along lines normal to the foil surface at several x/c at mid span, depicted in Figure 8, shows that once the flow reaches $x/c=0.35$ cavitation seldom reaches the foil surface, which is consistent with the sampling on the surface of the foil. Notably though, at this station along the foil cavity structures may be seen to be much thicker than they are closer to the leading edge. As one moves further downstream the cavities appear to move away from the foil and the mean density quickly increases to nearly pure water at $0.6 x/c$, which suggests that no cavitation structures make it this far downstream.

A crucial quantity of interest is the frequency with which the cavity sheet occurs and disappears in a cycle. In order to deduce this it is useful to examine the power spectral density functions of the unsteady lift

coefficient and total cavity volume present in the computational domain, as seen in Figures 9 and 10, respectively. Both of these quantities reveal prominent peaks at 38 Hz. The lift coefficient also shows significant peaks corresponding to higher harmonics of this fundamental frequency, but this is not observed for the cavity volume. In the experimental results this quantity was reported to be 32.5 Hz and numerical results from the 2011 SMP workshop ranged between 28 and 38 Hz (Hoekstra et al., 2011).

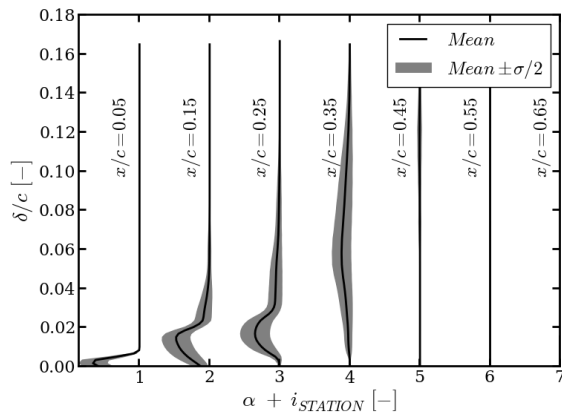


Figure 8: Mean value and standard deviation of the volume fraction along lines perpendicular to the foil surface at mid-span, sampled at several x/c and plotted as a function of foil surface distance, δ .

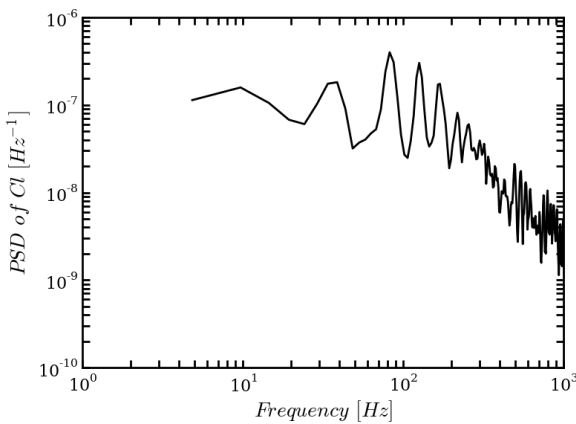


Figure 9: Power spectral density function of the lift coefficient.

Examining a fragment of the time trace of the total cavity volume, presented in Figure 11, shows that it follows a relatively sinusoidal behaviour, particularly at the lower volume fraction threshold which corresponds to regions of clearly-defined, coherent cavities. At higher

thresholds the curves show less dependence on the shedding frequency and yield much greater total cavity volumes, suggesting the presence of large regions of intermediate liquid fraction values.

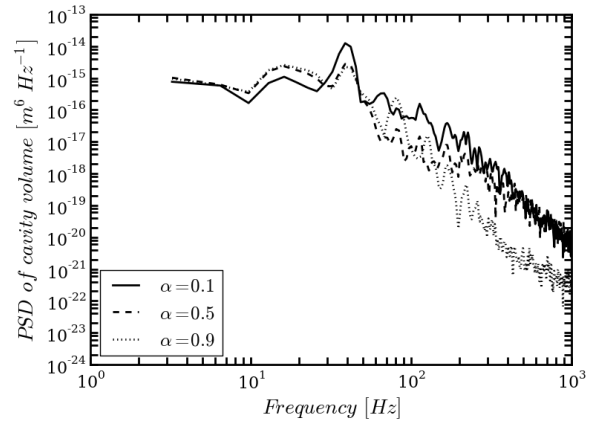


Figure 10: Power spectral density of the total cavity volume integrated up to different α thresholds.

Figure 12 presents distribution of the liquid volume fraction along a line normal to the foil surface at mid-span and x/c 0.15 over a period of time. One may note how during each of the four visible shedding cycles first an attached cavity is present. This then rapidly disappears, after which small, intermittent cavities pass through this location without touching the foil surface. The influence of the shedding frequency, corresponding to a period of about 26 milliseconds, may be seen in the data.

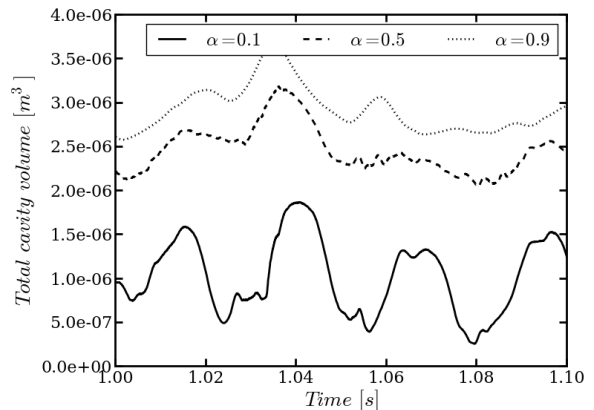


Figure 11: Chosen part of the total cavity volume time trace for three different volume fraction values.

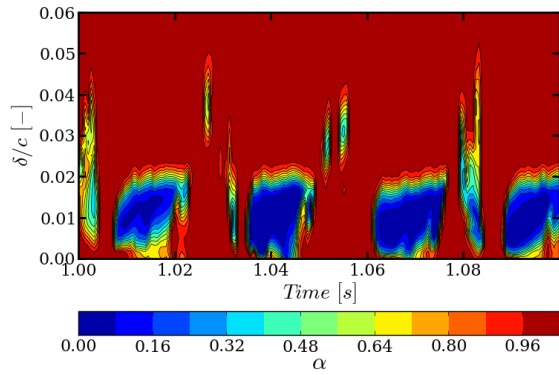


Figure 12: Temporal evolution of the volume fraction at mid-span and $x/c=0.15$ plotted as a function of foil surface distance, δ .

Figure 16 presents a series of consecutive instantaneous pictures showing cavitation extent in the original study by Foeth (2008) and the corresponding isocontours from the present simulation. One may note how a large, developed cavity sheet grows to its maximum size, then rapidly necks close to the leading edge due to the passage of a re-entrant jet, which is followed by the characteristic v-shaped notch in the sheet as it is filling with vapour again. One may see that the overall behaviour of the flow is similar to the one observed in the experiment. A major difference is that the stream-wise extent of the sheet is less in the present simulation, as already made evident from the surface pressure data. Likewise, cavitation does not extend as far span-wise. Because of this, the sheet is far more stable off-centreline than in the experiment, which leads to the re-entrant jet not occurring along the entire width of the sheet the way it was measured, but instead this behaviour may only be seen at the central part of the foil.

Cavitation - tunnel wall pressures

Figure 13 presents cavitation-induced pressure at the top wall of the virtual cavitation tunnel directly above the leading edge of the foil. The signal shows fluctuations of approximately $\pm 3\%$ of the reference pressure and, at the first glance, does not show direct dependence on the shedding frequency. However, spectral analysis, shown in Figure 14, indicates that the wall pressure is directly related to the cavity sheet behaviour and its higher harmonics.

Furthermore, data for other receivers placed along the centreline of the foil visible in Figure 14 shows that all of the investigated locations experience very similar pressure fluctuations. A closer analysis of how the peak value of the first harmonic varies with distance

from the leading edge of the foil is depicted in Figure 15. The magnitude of wall pressure fluctuations may be seen to decay with the distance from the location of the most prominent cavitation behaviour. Intuitively, one might expect this reduction in amplitude to follow an inverse square law, given that cavitation tends to act as a monopole noise source (Park et al., 2009b, Seol et al., 2005). Comparing the data to a least-squares quadratic fit indicates, however, that in the present data receivers closer to the leading edge do not see as much reduction in the fluctuations as could be expected.

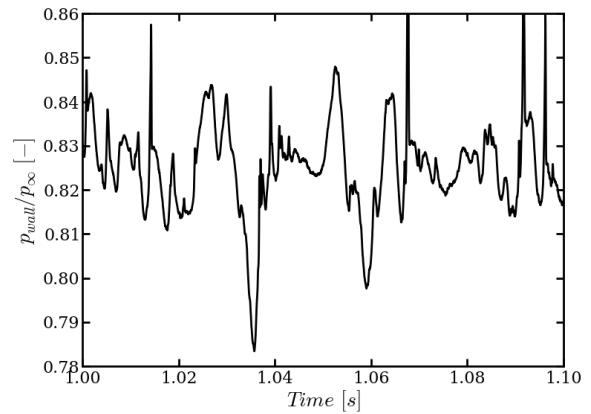


Figure 13: Wall pressure as a function of outlet pressure predicted for a probe above the leading edge of the foil at the centreline (probe 6).

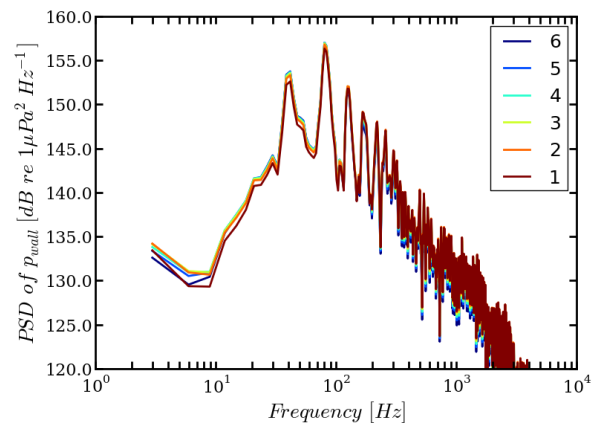


Figure 14: Power spectral density function of the wall pressure for a series of probes placed along the centreline of the foil, from the trailing edge (probe 1) to the leading edge (probe 6).

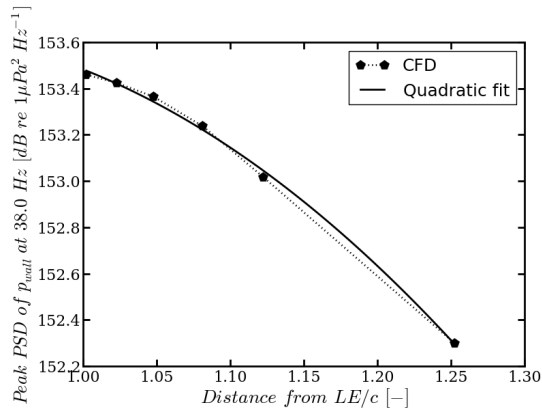


Figure 15: Decay of peak wall pressure PSD around the first harmonic (38 Hz) with distance from the foil leading edge, also showing a quadratic least-squares fit.

Lagrangian bubble tracking

Figure 17 shows the distribution of Lagrangian bubbles at an instant in the cavitation cycle similar to the one in Figure 16 g). One may note that the volume-of-fluid field behaves in a very similar when the hybrid model is used, yielding similar iso-contours. An important observation is also that while the baseline mass transfer model fails to convect cavities down to the trailing edge to the foil, which was observed in the experiment, the hybrid model does this successfully.

Closer analysis of where the Lagrangian bubbles get created shows that there are two primary scenarios in which transfer from the Eulerian frame occurs. First, when a well-defined cavity with high vapour fraction significantly reduces in size. The second instance, by far appearing to be more common in the present simulation, is when there exists a region of intermediate vapour fraction values and when at some point, either by becoming physically separated or when local volume fractions exceeded the thresholds, a certain sub-region gets identified as a separate cavity by the reconstruction algorithm. In Figure 17 this may be seen to occur primarily close to the centre-line of the foil where large interface displacements and velocities take place, causing injection of relatively large Lagrangian bubbles, predominantly just after the occurrence of the re-entrant jet. This appears to stand in good agreement with the experimental observations. A second region where Lagrangian bubbles get created is at around 35% of span where the cavity sheet also experiences substantial deformations. This behaviour may also be seen in the experimental data (Figure 16 a) and c)), although more bubbles appear to have been created at this location during experimental tests. This discrepancy could be due to the unsteadiness of the volume fraction field being under-predicted and not necessarily shortcomings of the Euler-to-Lagrange transition algorithm.

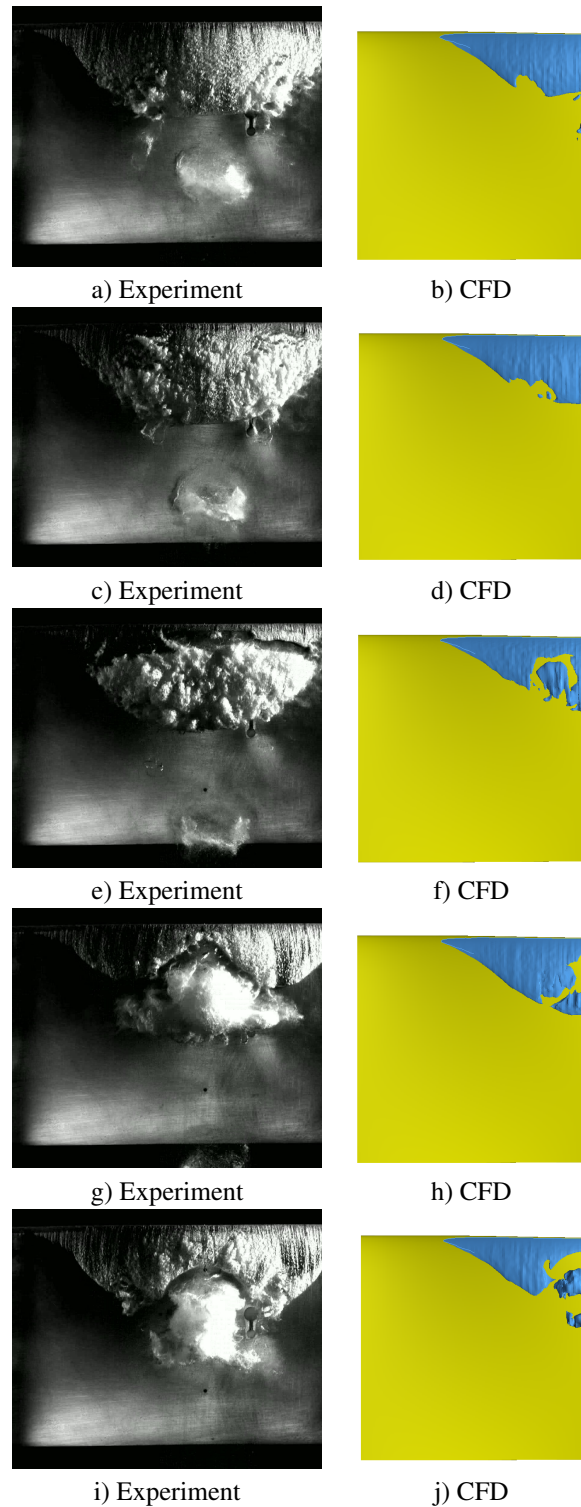
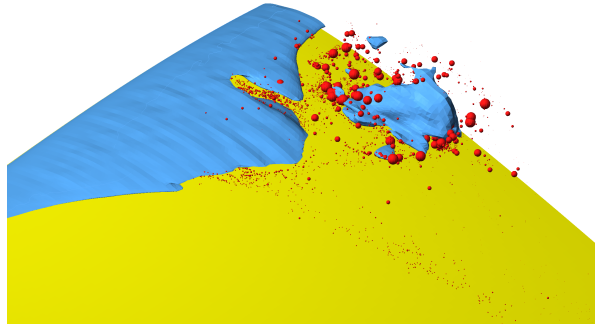


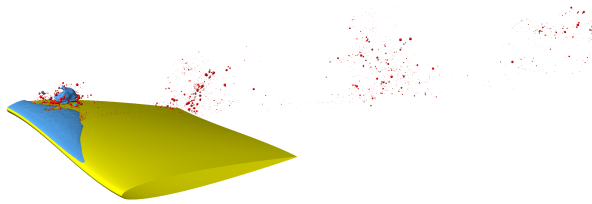
Figure 16: Flow snapshots of experimental data by Foeth (2008) and the iso-contours of the volume fraction field ($\alpha = 0.5$). CFD data only shows half of the foil, in accordance with how the calculation was set up.



a) Zoom-in on the leading edge



b) Top view (as in Figure 16 g) and h))



c) Isometric view showing the wake

Figure 17: View of an instantaneous distribution of Lagrangian bubbles (red spheres) and the fluid volume fraction (blue, $\alpha = 0.5$) at a point in the cavitation cycle similar to the one shown in Figures 16 g) and h).

A key aim of the present study was to investigate how much the Lagrangian bubbles contribute to the induced wall pressures, which is depicted in Figures 18 and 19 in the form of time- and frequency-domain plots. The former shows pressure at the probe above the leading edge of the foil over the duration of approximately one cavitation cycle. One may note that the pressure caused by the presence of small bubbles exhibits a broadband nature without immediately obvious concentrations along the time axis. One would expect that the spikes in the Eulerian pressure field, visible around times 0.006 and 0.012 s, to cause an increased likelihood of collapse of the Lagrangian bubbles, thus further reinforcing the predicted noise.

Turning to Figure 19 shows that including the pressure induced by the Lagrangian bubbles in the spectral analysis causes an 8 dB increase in the first harmonic

and makes the higher harmonics more clearly defined than when just the Eulerian pressure is considered. One may thus more readily see the relationship between the rise in local pressure causing an increased number of Lagrangian collapses and thus contributing more to the predicted wall pressures than in the time series in Figure 18. It should be noted that the low-frequency range of the spectra in Figure 19 is different than in Figure 14 is due to the hybrid model simulation having been run for a smaller number of cavitation cycles due to the increased computational cost.

In total, over 15000 Lagrangian bubbles have been introduced to the numerical domain over the period of 4 cavitation cycles. It has thus proven challenging to analyse their individual lifetimes in detail. An interesting hand-picked example is shown in Figure 20 where the time history of the evolution of the radius of a bubble and the external pressure acting on it are shown. One may note how first the bubble was in a region of constant pressure and thus experienced little variation in radius to the equilibrium assumption. It then experienced a rise in external pressure, leading to a decrease in radius. It was then swept closer to the centreline of the foil to a region of lower pressure, leading to a significant expansion, followed by a collapse and a series of rebounds. A sudden spike in the external pressure may then be seen which appears to have altered the oscillation frequency and reduced the amplitude of the radius. The bubble then was convected by the flow towards the outlet, which was accompanied by a steady rise in local pressure and decay of the oscillation of the radius.

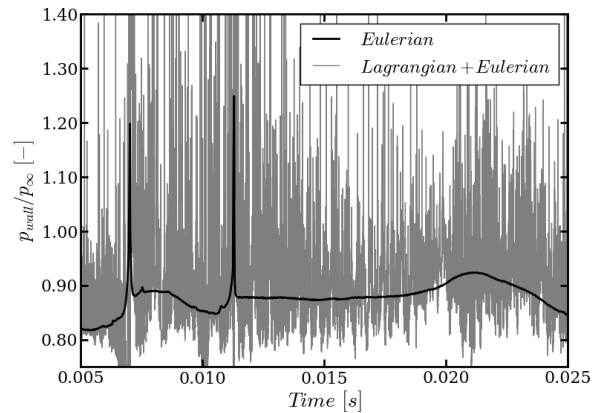


Figure 18: Direct Eulerian wall pressure at probe 6 also showing values with superimposed Lagrangian bubbles pressures.

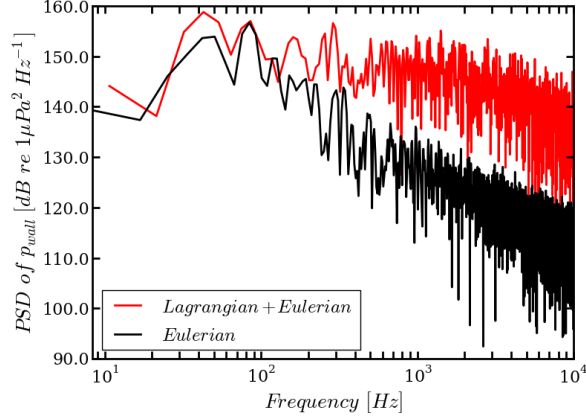


Figure 19: Power spectral density function of the direct CFD and combined Euler-Lagrange wall pressures at the location of probe 6.

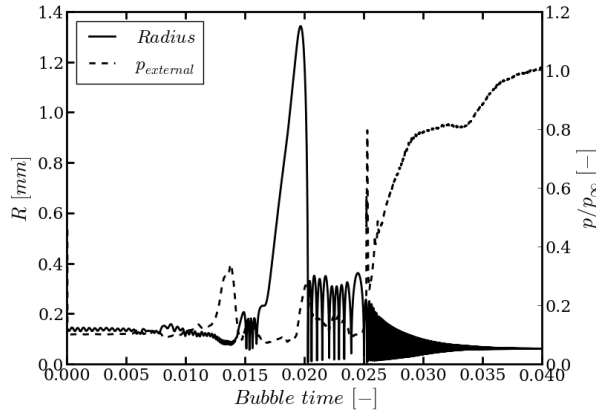


Figure 20: Time history of the radius and external pressure acting on a selected bubble which was created 0.1 s off-centreline close to the beginning of the simulation.

DISCUSSION

It has been shown, based on the distribution of pressure coefficient as well as the mean and instantaneous local values of the volume fractions, that the predicted cavitation extents are smaller than what was reported in the experimental data. The predicted shedding frequency of 38 Hz is also higher than 32.5 Hz originally measured by Foeth (2008). It is likely that both of these discrepancies are due to the same underlying issue, since a more pronounced cavity sheet could be expected to take more time to grow to its full extent, which would then lower the frequency of the complete cycle. It has been seen that the predicted steady-state solution is grid-independent, both in terms of forces and local pressure coefficient, although discrepancies have been observed in the lift being

too low compared to the experimental data and the minimum pressure coefficient being higher than in other numerical studies. This could potentially explain the under-prediction of cavitation extent. On the other hand, the study by Bensow (2011) also reported under-prediction of the cavity extents while quoted shedding frequencies closer to the experimentally measured value. Another possible reason for the current discrepancies could be the simplification made when assuming a constant nuclei size and density, which would not have been true in reality, or slight misalignment of the foil in the tunnel during the tests. Further sensitivity studies are therefore needed to truly explore the origin of this behaviour. Nonetheless, enough agreement may be seen between the present and publicly available data to support subsequent discussion.

As expected, the wall pressures induced by the cavitation were predicted to be primarily dependent on the shedding frequency. The data did also show, however, a substantial amount of higher harmonics, most likely associated with more local phenomena, such as formation of smaller clouds and local velocities of the cavity interface. This hints at the importance of three-dimensional effects in examining cavitation induced pressures. On this note, it has also been seen that while from a far-field perspective the cavitation-related noise source may be compact, in the near-field this is not necessarily the case.

Comparison of the predicted and experimentally observed distribution and location of Lagrangian bubbles during the cavitation cycle has revealed promising agreement. This indicates that, despite the simplicity of its current implementation, the hybrid Eulerian-Lagrangian cavitation model accounts for the dominant physical phenomena. A key observation in this regard has been the importance of local cavity interface deformations, most likely related to the presence of shear layers, on where regions of intermediate volume fractions occur and spawn potential injection sites for Lagrangian bubbles. Although no experimental data exist in the public domain to validate the predicted wall pressures, the observed broadband contributions of the small-scale bubbles superimposed on the underlying low-frequency oscillations induced by the large-scale cavity sheet and clouds stand in qualitative agreement with what is understood about multi-scale cavitation noise (Brennen, 2009a, Bretschneider et al., 2008, Matusiak, 1992).

Several areas for improvement have been identified in the current multi-scale cavitation model. It has been seen that certain Lagrangian bubbles grow in size greater than the local grid size, which would justify transferring them back to the Eulerian frame of reference (Hsiao et al., 2014). Likewise, a small number of the Lagrangian bubbles were seen to come in contact with the cavities defined by the volume of fluid. In reality,

one would expect the smaller bubbles to merge with their larger counterpart or at least interact with the cavity interface, which is not accounted for at the moment. The same goes for the interaction of Lagrangian bubbles between themselves (Vallier, 2013). The latter is, however, expected to be computationally expensive due to the added cost of a global reduce operation required for bubbles in each sub-domain to contain information on all the other Lagrangian parcels in the simulation. Finally, it has been seen that a vast amount of data gets generated from the Lagrangian tracking algorithm which makes it difficult to utilise using more basic CFD post-processing techniques. It is thus hoped that more robust and statistically sound approaches can be devised in the future to better inform the user on what the results mean in practice.

CONCLUSIONS

The present multi-scale cavitation model predicts cavitation behaviour which stands in qualitative agreement with the experimental observations. The broadband noise induced by the Lagrangian cavities was not predicted to affect the dominant, low-frequency harmonics of the wall pressures significantly, but was observed to extend the range of frequencies generated by cavitation well above a kilohertz. It is believed that, following the inclusion of several additional physical mechanisms, the current model will form a useful tool for cross-examination of cavitation tunnel noise measurements and will contribute towards a better understanding of ship noise.

ACKNOWLEDGEMENTS

The authors would like to acknowledge the use of the Iridis 4 supercomputer of University of Southampton, UK, on which the discussed simulations have been conducted.

REFERENCES

- Aktas, B., Turkmen, S., Sampson, R., Shi, W., Fitzsimmons, P., Korkut, E., and Atlar, M., "Underwater radiated noise investigations of cavitating propellers using medium size cavitation tunnel tests and full-scale trials," Fourth International Symposium on Marine Propulsors (SMP), Austin, Texas, USA, June, 2015.
- Bensow, R., "Simulation of the unsteady cavitation on the the Delft Twist11 foil using RANS, DES and LES," 2nd International Symposium on Marine Propulsors, Hamburg, Germany, June, 2011.
- Bertschneider, H., Bosschers, J., Choi, G. H., Ciappi, E., Farabee, T., Kawakita, C., and Tang, D., "Specialist Committee on Hydrodynamic Noise," Technical report, ITTC, 2014.
- Brennen, C. E., "Cavitation," Fundamentals of Multiphase Flow, chapter 5, pages 97–115. Cambridge University Press, Cambridge, 2 edition, 2009a ISBN 978-0-521-13998-4.
- Brennen, C. E., "Bubble growth and collapse," Fundamentals of Multiphase Flow, chapter 4, pages 73–96. Cambridge University Press, Cambridge, 2 edition, 2009b ISBN 978-0-521-13998-4.
- Bretschneider, H., Lydorf, U., and Johannsen, C., "Experimental Investigation to Improve Numerical Modeling of Cavitation," Technical report, HSWA GmbH, 2008.
- Brooker, A. and Humphrey, V. F., "Measurement of Radiated Underwater Noise from a Small Research Vessel in Shallow Water," A. Yücel Odabas Colloquium Series, pages 47–55, 6th-7th November, Istanbul, Turkey, 2014.
- Chahine, G., "Nuclei effects on cavitation inception and noise," 5th Symposium on Naval Hydrodynamics, pages 8–13, St. John's, Newfoundland and Labrador, Canada, August, 2004.
- EU FP7, "AQUO Project," 2014a URL <http://www.aquo.eu/>.
- EU FP7, "SONIC Project," 2014b URL <http://www.sonic-project.eu/>.
- Foeth, E. J., Doorne, C. W. H., van Terwisga, T., and Wieneke, B., "Time resolved PIV and flow visualization of 3D sheet cavitation," Experiments in Fluids, 40(4):503–513, 2006 ISSN 0723-4864 doi: 10.1007/s00348-005-0082-9.
- Foeth, E., "The structure of three-dimensional sheet cavitation," PhD thesis, TU Delft, 2008.
- Hildebrand, J., "Anthropogenic and natural sources of ambient noise in the ocean," Marine Ecology Progress Series, 395:5–20, dec 2009 ISSN 0171-8630 doi: 10.3354/meps08353.
- Hoekstra, M., van Terwisga, T., and Foeth, E. J., "SMP11 Workshop - Case 1: DelftFoil," Second International Symposium on Marine Propulsors, Hamburg, Germany, 2011.
- Hsiao, C., Ma, J., Chahine, G. L., Ynaflow, D., and Nc, I., "Multi-Scale Two-Phase Flow Modeling of Sheet and Cloud Cavitation," 30th Symposium on Naval Hydrodynamics, Hobart, Tasmania, Australia, 2-7 November, 2014.
- Hsiao, C. T. and Chahine, G. L., "Scaling of tip vortex cavitation inception for a marine open propeller," 27th Symposium on Naval Hydrodynamics, Seoul, Korea, October, 2008.

- Ianniello, S., Muscari, R., and Mascio, A., "Ship underwater noise assessment by the acoustic analogy. Part I: nonlinear analysis of a marine propeller in a uniform flow," Journal of Marine Science and Technology, 18(4):547–570, jul 2013 ISSN 0948-4280 doi: 10.1007/s00773-013-0227-0.
- Ianniello, S. and Bernardis, E. D., "Farassat's formulations in marine propeller hydroacoustics," International Journal of Aeroacoustics, 14(1 & 2):87–103, 2015.
- Koop, A. H., "Numerical simulation of unsteady three-dimensional sheet cavitation," PhD thesis, University of Twente, Enschede, The Netherlands, 2008.
- Lidtke, A. K., Turnock, S. R., and Humphrey, V. F., "Characterisation of sheet cavity noise of a hydrofoil using the Ffowcs Williams-Hawkings acoustic analogy," Computers & Fluids, 130:8–23, 2016 doi: 10.1016/j.compfluid.2016.02.014.
- Lloyd, T. P., Lidtke, A. K., Rijpkema, D., Van Wijnngaarden, E., Turnock, S. R., and Humphrey, V. F., "Using the FW-H equation for hydroacoustics of propellers," Numerical Towing Tank Symposium (NuTTS), Cortona, Italy, 2015.
- Matusiak, J., "Pressure and noise induced by a cavitating marine screw propeller," PhD thesis, Helsinki University of Technology, 1992.
- Menter, F. R., Kuntz, M., and Langtry, R., "Ten Years of Industrial Experience with the SST Turbulence Model," Hanjalic, K., Nagano, Y., and Tummers, M., editors, Turbulence, Heat and Mass Transfer 4, pages 625 – 632, Antalya, Turkey, 12-17 October, 2003. Begell House, Inc.
- Nordin, N. P. A., "Complex chemistry modelling of diesel spray combustion," PhD thesis, Chalmers University of Technology, 2001.
- Park, C., Seol, H., Kim, K., and Seong, W., "A study on propeller noise source localization in a cavitation tunnel," Ocean Engineering, 36(9-10):754–762, jul 2009a ISSN 00298018 doi: 10.1016/j.oceaneng.2009.04.005.
- Park, K., Seol, H., Choi, W., and Lee, S., "Numerical prediction of tip vortex cavitation behavior and noise considering nuclei size and distribution," Applied Acoustics, 70(5):674–680, may 2009b ISSN 0003682X doi: 10.1016/j.apacoust.2008.08.003.
- Plesset, M. S. and Prosperetti, A., "Bubble dynamics and cavitation," Annual Review of Fluid Mechanics, 9(1): 145–185, 1977.
- Sauer, J. and Schnerr, G. H., "Development of a new cavitation model based on bubble dynamics," Zeitschrift für Angewandte Mathematik und Mechanik, 81:561–562, 2001.
- Seo, J. H., Moon, Y. J., and Shin, B. R., "Prediction of cavitating flow noise by direct numerical simulation," Journal of Computational Physics, 227(13):6511–6531, jun 2008 ISSN 00219991 doi: 10.1016/j.jcp.2008.03.016.
- Seol, H., "Time domain method for the prediction of pressure fluctuation induced by propeller sheet cavitation: Numerical simulations and experimental validation," Ocean Engineering, 72:287–296, nov 2013 ISSN 00298018 doi: 10.1016/j.oceaneng.2013.06.030.
- Seol, H., Suh, J.-C., and Lee, S., "Development of hybrid method for the prediction of underwater propeller noise," Journal of Sound and Vibration, 288(1-2):345–360, nov 2005 ISSN 0022460X doi: 10.1016/j.jsv.2005.01.015.
- Spalart, P. R. and Allmaras, S. R., "A one equation turbulence model for aerodynamic flows," AIAA Journal, 94 (439), 1992.
- Sunil, M., Keith, T. G., and Nikolaidis, E., "Numerical simulation of traveling bubble cavitation," International Journal of Numerical Methods for Heat & Fluid Flow, 16 (4):393–416, 2006.
- Tomar, G., Fuster, D., Zaleski, S., and Popinet, S., "Multiscale simulations of primary atomization," Computers and Fluids, 39(10):1864–1874, 2010 ISSN 00457930 doi: 10.1016/j.compfluid.2010.06.018.
- Tomita, Y. and Shima, A., "On the behavior of a spherical bubble and the impulse pressure in a viscous compressible liquid," Bulletin of the JSME, 20(149):1453–1460, 1977.
- Urik, R. J., "Ambient noise in the sea," Technical report, 1984.
- Vallier, A., "Simulations of cavitation-from the large vapour structures to the small bubble dynamics," PhD thesis, Lund University, 2013.
- Wu, X. C., Wang, Y. W., and Huang, C. G., "Effect of mesh resolution on large eddy simulation of cloud cavitating flow around a three dimensional twisted hydrofoil," European Journal of Mechanics B / Fluids, 55:229–240, 2016 doi: 10.1016/j.euromechflu.2015.09.011.
- Yakubov, S., Cankurt, B., Abdel-Maksoud, M., and Rung, T., "Hybrid MPI/OpenMP parallelization of an Euler-Lagrange approach to cavitation modelling," Computers and Fluids, 80(1):365–371, 2013 ISSN 00457930 doi: 10.1016/j.compfluid.2012.01.020.

DISCUSSION

Rickard Bensow, Professor, Chalmers University of Technology, Gothenburg, Sweden

The authors present a well written and interesting paper on the application of a hybrid Eulerian-Lagrangian cavitation modelling approach for pressure pulse simulations. The idea of how to develop the modelling itself is not new, but the paper presents a comprehensive description of the authors interpretation and implementation and a nice application.

1. The addition of the Lagrangian bubbles is motivated by the intrinsic inability of an incompressible Eulerian approach to account for cavity collapse behaviour and thus its broad band contribution. I agree on this, but perhaps one could have commented that there are other contributions to broad band noise/pressure pulses (in sheet or tip cavity dynamics) that the Eulerian method has better potential to capture; an argument actually strengthening the hybridisation.
2. As I interpret the methodology, its a one-way coupling such that the Eulerian simulation determines the flow pressure field, while the integration of the pressure from Lagrangian bubble dynamics is only used to sample at the probe location. Is this correct? If so, could the authors comment on how a two way coupling could be realised and how it would affect the flow results?
3. Regarding the discrepancy in lift coefficient, there has been numerical results published which give better agreement with experiments than was reported at the 2011 SMP workshop. As the mesh study indicated well converged results, my guess would be that this is then a result of the turbulence model chosen. It would thus be interesting to see an additional run with an alternative model.
4. It would be interesting to see the sheet cavity outline in relation to the mesh resolution on the suction side of the foil. I suspect that the mesh resolution, although fine at 7.3 M cells for half foil and certainly good enough for wetted flow, is too low around the sheet and that this, then, is one reason for the under predicted cavity extent. As nicely pointed out by the authors, the transported shed vapour seem to be captured by the Lagrangian bubbles, but the sheet dynamics may be hampered by the seemingly low resolution a bit of the foil surface.

I enjoyed reading the paper with its well presented content and Im much looking forward to further discussion at the symposium.

AUTHORS' REPLY

We would like to thank the discussor for the insightful comments which increased the value of the paper. Specific questions and remarks are addressed below.

Question 1: The discussor raises a very important point and the original discussion in the paper oversimplified the problem to a degree. It has been shown in the literature that collapsing cavity sheets and tip cavitation may contribute to the broadband noise spectrum but a pure Lagrangian approach would likely be insufficient to resolve these accurately.

Question 2: The summary of the method provided by the discussor is correct - the initial model presented in the paper assumed the Lagrangian bubbles to be convected by the fluid with the assumption that their volume fraction is relatively low. This was later found not to be true at all times, as may be seen, for instance, in Figure 17. It shows that often the bubbles cluster together in relative proximity and sometimes grow in size considerably, as seen in Figure 20. This implies that interactions between bubbles and the action of the Lagrangian bubbles on the flow should be considered in order to achieve more accurate modelling.

Including a source term in the momentum equation could relatively easily be added to reflect the change in momentum of the fluid caused by it carrying a mass of Lagrangian bubbles. Furthermore, one could also implement an algorithm searching the neighbourhood of each particle for other bubbles. In case a collision was detected, semi-empirical criteria could be used in order to determine whether the bubbles will coalesce or bounce, and how this interaction will occur. A detailed discussion of the topic is given, for instance, by Vallier (2013).

Question 3: The reviewer is right to point out that there have been several more recent studies reporting better agreement with the experimental values. For instance, Wu *et al.* Wu et al. (2016) used wall-modelled LES on a 10 million cells grid and achieved very good agreement with the experimental values in the non-cavitating condition (authors did not report on the forces predicted for cavitation conditions). Since in the present simulations the solution is deemed grid-independent future work will have to focus on identifying the exact reason for the observed discrepancies, most likely associated with the turbulence model.

Following the presented simulations two additional runs were carried out on the 7.3 M grid using LES with the Smagorinsky model and an implicit model (ILES). The

present mesh was too coarse for LES to resolve the near-wall region, with resolution lacking in the x- and z-directions, and thus a wall model was used. Both of the simulations predicted similar lift coefficient values as well as very comparable flow features. The studies were preliminary in nature and so the answers they provided must be treated with caution, but they do point to the Eulerian cavitation model and its settings being responsible for the observed discrepancies.

Question 4: A closer view of the mesh in the vicinity of cavitation is presented in Figure 21. It shows that the grid is quite fine close to the surface of the foil but expands in the size further away. When moving downstream the shed clouds just about cross into the coarser region which may have affected how far downstream they could have been convected in the presented simulation. We think, however, that the key region responsible for the shedding frequency lies closer to the foil and thus should not be greatly affected by discretisation errors.

In order to further explore the discussor's observation, unsteady cavitating simulations were carried out on variations of the baseline grid with additional refinement in the span-wise and stream-wise directions, particularly on

the upper foil surface. The largest mesh used contained a little over 21 million cells. As could be expected, finer resolution allowed a greater amount of flow detail to be captured but the overall sheet dynamics remained comparable and exhibited similar frequency of shedding between 38 and 40 Hz, depending on the mesh used.

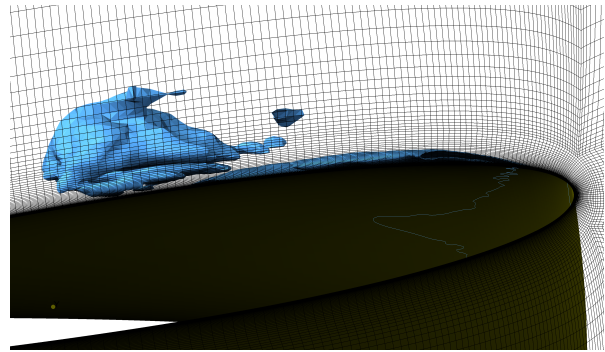


Figure 21: Close-up view of the 7.3 million element mesh at the centreline of the foil also showing an instantaneous extent of cavitation at a time when the shed cloud is the largest.